Ion Transport in Electrically Imperfect Nanopores

*Yechan Noh and Narayana R. Aluru**

Department of Mechanical Science and Engineering, Beckman Institute for Advanced Science and Technology, University of Illinois at Urbana-Champaign, Urbana, Illinois 61801, United States

*E-mail: aluru@illinois.edu

ABSTRACT

Ionic transport through a charged nanopore at low ion concentration is governed by the surface conductance. Several experiments have reported various power-law relations between the surface conductance and ion concentration, *i.e.,* $G_{\mathrm{surf}} \propto c_0^{\alpha}$. However, the physical origin of the varying exponent, α, is not yet clearly understood. By performing extensive coarse-grained Molecular Dynamics (MD) simulations for various pore diameters, lengths, and surface charge densities, we observe varying power-law exponents even with a constant surface charge and show that α depends on how electrically "perfect" the nanopore is. Specifically, when the net charge of the solution in the pore is insufficient to ensure electroneutrality, the pore is electrically "imperfect" and such nanopores can exhibit varying α depending on the degree of "imperfectness". We present an ionic conductance theory for electrically "imperfect" nanopores that not only explains

the various power-law relationships but also describes most of the experimental data available in the literature.

KEYWORDS

ion transport, nanopore, power-law, ion conductance, ion selectivity, surface charge, molecular dynamics

The distinctive characteristics of micro and nanoscale ion transport have been utilized extensively for various applications in science and engineering. The surface-charge-governed ion transport[1] theory has been used, in conjunction with experimental ionic conductance data at low concentration, to estimate the surface charge density of a nanopore/channel.[2–4] Furthermore, the dimensions of the nanoscale conduit, which are not easy to measure due to their tiny scale, have been determined by using the ion transport theory on measured current data.[5–7] The molecular-level sensitivity of ion transport through an ultra-thin nanopore has greatly contributed to advances in DNA sequencing and translocation technologies.[8–11] Biological organisms take advantage of selective ion transport to maintain metabolism.[12] Molecular scale separation of ions[13,14] and electricity generation using osmotic energy[3,15] have also been actively studied. Despite the importance of ion transport phenomena, there is still a considerable knowledge gap in the scaling behavior of ion conductance (the power-law relation between conductance and concentration is given by, $G \propto c_0^{\alpha}$). Generally, at high ionic concentration, the ion transport is governed by the bulk transport mechanism where the exponent $\alpha = 1$ holds. On the other hand, at low concentration, the ion transport is dominated by the surface transport mechanism. In this regime, various scaling laws ($0 \leq \alpha \leq 1$) have been reported in different experimental settings

over the past few years. However, the physical origins of the various scaling laws are not clearly understood.

The scaling behavior of ion transport has been studied extensively since the cornerstone work done by Stein *et al.*[1] In this work, the conductance saturation ($\alpha \approx 0$) was observed in silica-oxide micro-nano channels. They have shown that at low concentration the transport is dominated by counterions that accumulate near the charged surface to maintain electroneutrality. In subsequent work, Smeets *et al.*[16] observed that the conductance does not saturate ($\alpha \sim 0.3$) in their silica-oxide nanopores. This non-zero exponent was explained by a variable-charge model (referred to as charge regulation) where the surface charge density was considered to change as a function of ion concentration in reservoir. Secchi *et al.*[17] observed that the conductance in CNTs exhibited $\alpha \sim 1/3$ scaling law for all the tested diameters (3.5 nm ~ 35 nm) and pH (4 ~ 10). They also suggested charge regulation as a possible interpretation of this scaling-law and derived the $\alpha = 1/3$ scaling law using the Gouy-Chapman model.[18,19] Similarly, Biesheuvel and Bazant[20] derived the power-law, $\alpha = 1/2$, by using charge regulation with Langmuir isotherm. Uematsu *et al.*[21] showed that the crossover among the power-laws ($\alpha = 0$, $1/3$ and $1/2$) depends on the ion concentration and pH. Manghi *et al.*[22] analytically arrived at the scaling of $\alpha = 1/2$, $1/3$ and $2/3$ by introducing charge regulation and slip.

However, not only those exponents, almost any power-law exponent ranging from $0 \leq \alpha < 1$ have been observed in prior studies on graphene nanopores,[23–25] graphene Al_2O_3 pores,[26] silica nitride pores,[27] silica oxide nanochannels/pores,[16,28,29] CNT,[17,30] wCNTPs,[31] and biological nanopores.[32] To elucidate the physical origin of the various exponents, we performed extensive coarse-grained MD simulations where explicit ions and implicit solvent are used. The results show that depending on the geometry of the pore, the electroneutrality in the pore region may not

be satisfied and the electrical potential in the pore due to surface charge leaks into the reservoir. Considering the leakage of surface potential, we develop an ion conductance theory that describes the various power-law exponents and the theory is shown to accurately predict MD as well as experimental data.

RESULTS AND DISCUSSION

Electrophoretic conductance and access resistance

The ionic conductance through a charged nanopore is enhanced, when compared to the bulk conductance, due to the diffuse layer transport near the pore surface. In a cylindrical pore with a 1:1 electrolyte and $\mu = \mu_+ = \mu_-$, the enhanced electrophoretic transport can be modeled as

$$G_{\mathrm{ph}} = 2Fc_0\mu\sqrt{1+\tilde{\sigma}^2}\left(\frac{L}{\pi R^2}\right)^{-1}, \tag{1}$$

where F is the Faraday constant, μ is the ion mobility (in $\mathrm{m^2 s^{-1} V^{-1}}$), c_0 is the reservoir concentration (in $\mathrm{mol \cdot m^{-3}}$), L is the length of the pore, and R is the pore radius. Eq (1) can be derived from the Space-Charge (SC) theory[33,34] with Donnan equation[17,20] or from the electro-chemical equilibrium (the mean-field Poisson-Boltzmann theory)[35,36] with the electroneutrality assumption in the pore. We introduce a dimensionless number $\tilde{\sigma}$ as the ratio between the net charge concentration required in the pore for electroneutrality and the charge concentration of the bulk solution, *i.e.,* $\tilde{\sigma} \equiv \frac{q_+\langle c_+\rangle_{\mathrm{EN}} + q_-\langle c_-\rangle_{\mathrm{EN}}}{(q_+ - q_-)c_0}$, where $q_\pm$ is the charge of cation/anion, $\langle c_\pm\rangle_{\mathrm{EN}}$ is the ensemble averaged concentration of cation/anion for the Electrically Neutral (EN) condition. For a 1:1 electrolyte and homogeneous charge distribution in a cylindrical pore, the dimensionless parameter can be rewritten as

$$\tilde{\sigma} = \frac{-\sigma}{Fc_0R}, \tag{2}$$

where σ is the surface charge density (in $\mathrm{C/m^2}$). Note that the Dukhin number,[27,35,37] $\mathrm{Du} = \frac{\kappa_{\mathrm{surf}}}{R\kappa_{\mathrm{bulk}}}$, is equal to $|\tilde{\sigma}|$ when electroosmosis is ignored, where κ_{surf} is the surface conductivity and κ_{bulk} is the bulk conductivity. The sign of $\tilde{\sigma}$ is an opposite sign of surface charge and this facilitates to consider the direction of surface current. The absolute value of $\tilde{\sigma}$ provides an important interpretation of the ion transport mechanism. When $|\tilde{\sigma}| \ll 1$ (generally at high c_0), Eq 1 reduces to the bulk conductivity limit, *i.e.,* $\kappa_{\mathrm{bulk}} = 2Fc_0\mu$. When $|\tilde{\sigma}| \gg 1$ (generally at low c_0), Eq 1 reduces to the surface-charge-governed conductivity limit, *i.e.,* $\kappa_{\mathrm{surf}} = |\tilde{\sigma}|\kappa_{\mathrm{bulk}} = \frac{2\mu|\sigma|}{R}$, which is independent of the reservoir concentration.[1] The summation of these two limits of Eq 1 is taken to be the electrophoretic conductance as suggested by earlier works:[2,38,39]

$$G_{\mathrm{ph}} \approx G_{\mathrm{bulk}} + G_{\mathrm{surf}} = 2Fc_0\mu(1 + |\tilde{\sigma}|)\left(\frac{L}{\pi R^2}\right)^{-1}. \tag{3}$$

Eq 3 provides insights into bulk and surface transport mechanism. Nonetheless, Eq 1, where the bulk and surface transport occur as a coupled mechanism, is physically accurate compared to Eq 3, where the bulk and surface transport are decoupled and assumed to be independent of each other. Both Eq 1 and Eq 3 are suitable for long ($L \gg R$) nanopores where the access resistance is negligible. For nanopores with $L \sim R$, the access resistance needs to be included in the conductance model. The access resistance can be modeled by the Maxwell-Hall access resistance, $R_{\mathrm{Hall}} = \frac{1}{2\kappa R}$.[40–42] By introducing the Maxwell-Hall access resistance, the electrophoretic conductance can be written as,

$$G_{\mathrm{ph}} = 2Fc_0\mu\sqrt{1 + \tilde{\sigma}^2}\left(\frac{L}{\pi R^2} + \frac{1}{2R}\right)^{-1}. \tag{4}$$

We can also simply express the conductance as $G = \kappa\left(\frac{L}{\pi R^2} + \frac{1}{2R}\right)^{-1}$, where κ is the conductivity.[24,43,44] Note that, Eq 4 reduces to Eq 1 in the limit of $L \gg R$. We compared the

model in Eq 4 with MD simulations using implicit water for various pore geometries and surface charges. The surface charge density in MD is assumed to be constant with respect to the reservoir concentration, *i.e.,* no charge regulation is used. The details of the coarse-grained MD simulation are given in the Methods Section. Note that both Eq 4 and the coarse-grained MD simulation only consider the electrophoretic ion transport. Figure 1 shows that Eq 4 agrees well with the MD data only in the bulk transport dominant regime $c_0 \gg \frac{|\sigma|}{FR}$, (*i.e.,* $c_0 \gg 0.23$ M for the cases in Figure 1A). Note that if the access resistance is omitted (*i.e.,* Eq 1), the model does not accurately predict the bulk conductance for short pores ($L \lesssim R$) (see Figure S1). In the regime where the surface conductance is dominant ($c_0 \ll \frac{|\sigma|}{FR}$), Eq 4 deviates from the MD data. These discrepancies are greater for short pores (L is small). For a constant surface charge, the conductance model in Eq 4 predicts the conductance saturation ($G =$ constant) at low c_0. According to MD simulation, however, even at low concentration, the conductance decreases continuously as the reservoir concentration decreases following the power-law, $G_{\text{surf}} \propto c_0^{\alpha}$ (*i.e.,* linear $\log(G)$ - $\log(c_0)$ curve).

Electrophoretic conductance with electric-potential-leakage

To understand the physical origin of the various power-law exponents, we examined if electroneutrality is maintained in the pore as assumed in Eq 4. Figure 2 shows the distribution of the net charge of solution along the axial coordinate of the pore normalized by the pore length. In all the tested cases, the net charge of solution in the pore is insufficient to maintain the electroneutral condition, $\langle c_+ \rangle_{\text{EN}} - \langle c_- \rangle_{\text{EN}} = 2c_0\tilde{\sigma}$. This deficiency of net charge is worse at the pore edges. Similar phenomena, referred to as *charge overspill*, *end effects,* and *electroneutrality breakdown* have been reported.[45–47] It should be noted that the lack of electroneutrality in the

pore region does not indicate that the electroneutrality of the whole system fails. The electroneutrality of the entire system is maintained by the combination of the net charge of solution in the pore and that of in the reservoir. The physical origin of the net charge deficiency in the pore is the leakage of the surface-electric-potential (electric potential due to the surface charge density of the pore) into the reservoir, where the leaked electric potential does not contribute to the surface conductance. To incorporate the leakage of surface-electric-potential into the conductance model, the electrochemical equilibrium between the reservoir and pore is considered, for a 1:1 electrolyte, as

$$\zeta_{\pm} + k_{\mathrm{B}}T \log c_0 = \zeta_{\pm} + k_{\mathrm{B}}T \log\langle c_{\pm}\rangle_{\mathrm{p}} \pm e\bar{\psi}_{\mathrm{p}}, \tag{5}$$

where $\zeta_{\pm}$ is the chemical potential of a cation (ζ_{+}) and anion (ζ_{-}), k_{B} is the Boltzmann constant, T is the temperature, $\langle c_{\pm}\rangle_{\mathrm{p}}$ is the ensemble averaged concentration of a cation/anion in the pore without electroneutrality assumption and $\bar{\psi}_{\mathrm{p}}$ is the mean potential in the pore. First, if there is no leakage of surface-electric-potential, the mean potential $\bar{\psi}_{\mathrm{p}}$ is equal to the Donnan potential, $\bar{\psi}_{\mathrm{D}}$. From Eq 5 and the electroneutrality condition, the Donnan potential is described as[35]

$$\bar{\psi}_{\mathrm{D}} = \frac{k_{\mathrm{B}}T}{e} \log\left(\sqrt{1+\tilde{\sigma}^2} - \tilde{\sigma}\right). \tag{6}$$

If the surface-electric-potential leaks, the mean potential in the pore is smaller than the Donnan potential, $\bar{\psi}_{\mathrm{p}} < \bar{\psi}_{\mathrm{D}}$.[48] In this case, the pore potential can be modeled as

$$\bar{\psi}_{\mathrm{p}} \equiv (1-\alpha)\bar{\psi}_{\mathrm{D}}, \tag{7}$$

where α is the fraction of the surface-electric-potential that leaks out of the pore: $\alpha = 0$ means no leakage and $\alpha = 1$ means perfect leakage. Combining Eqs 5-7, the ensemble averaged concentration in the pore is derived as

$$\langle c_{\pm} \rangle_{\mathrm{p}} = c_0 \left(\sqrt{1 + \tilde{\sigma}^2} \pm \tilde{\sigma} \right)^{1-\alpha}. \tag{8}$$

The electrophoretic conductivity is given by,

$$\kappa_{\mathrm{ph}} \approx F \left(\mu_+ \langle c_+ \rangle_{\mathrm{p}} + \mu_- \langle c_- \rangle_{\mathrm{p}} \right). \tag{9}$$

The mean-field approximation in Eq 9 is acceptable for pores with diameters larger than 3 nm and for moderate surface charge where the mobility of ions is nearly invariant near the surface. The mobility of ions in highly confined pores is typically lower than the bulk value. However, this effect can usually be neglected for pores larger than 3 nm.[49] Under these assumptions, modeling the pore conductivity can be simplified into modeling ion concentration in the pore. From Eq 8 and 9, the nanopore conductivity is given by,

$$\kappa_{\mathrm{ph}} = F c_0 \left\{ \mu_+ \left(\sqrt{1 + \tilde{\sigma}^2} + \tilde{\sigma} \right)^{1-\alpha} + \mu_- \left(\sqrt{1 + \tilde{\sigma}^2} - \tilde{\sigma} \right)^{1-\alpha} \right\}. \tag{10}$$

The conductivity model presented in Eq 10 includes two types of transport mechanisms in a coupled form; one is bulk transport, where $\kappa_{\mathrm{bulk}} \propto c_0$ and the other is the surface transport, where $\kappa_{\mathrm{surf}} \propto c_0^{\alpha}$ (see Figure 3A). In case $\alpha = 0$ (electrically perfect nanopore), the conductivity saturates as reservoir concentration decreases. If $\alpha = 1$ (no surface-electric-potential is present in the pore), Eq 10 reduces to the bulk conductivity. Similarly, if there is no surface charge, $|\sigma| = 0$, Eq 10 reduces to the bulk conductivity. The absolute value of the surface charge density, $|\sigma|$, is proportional to the magnitude of the surface conductivity (see Figure 3B). The conductivity model presented in Eq 10 fits well with the MD data for various lengths, diameters, and surface charge densities (see Figure S2).

For a cylindrical geometry, the ionic conductance can be described as the product of the geometrical parameters and ionic conductivity as, $G = \kappa \left(\frac{L}{\pi R^2} + \frac{1}{2R} \right)^{-1}$. Using Eq 10, the conductance can be written as

$$G_{\mathrm{ph}} = Fc_0\left\{\mu_+\left(\sqrt{1+\tilde{\sigma}^2}+\tilde{\sigma}\right)^{1-\alpha} + \mu_-\left(\sqrt{1+\tilde{\sigma}^2}-\tilde{\sigma}\right)^{1-\alpha}\right\}\left(\frac{L}{\pi R^2}+\frac{1}{2R}\right)^{-1}. \qquad (11)$$

We note that Eq 11 is a general form of conductance that can reproduce all the earlier conductance models (Eq 1, 3 and 4). Figure 1 shows that the theory given by Eq 11 compares well with the MD data for various lengths, diameters and surface charge densities. Figure 1A shows that the power-law exponent α of the surface conductance increases as the pore length decreases. Interestingly, Eq 11, as well as the MD data, predict that at very low concentrations, longer pores have higher conductance compared to shorter pores. Figure 1C shows that α decreases as the pore diameter decreases. Thus, the diameter and length of the pore have an opposite effect on α. Also, it is observed from MD that pores with different D and L but with the same D/L ratio, have nearly the same exponent, α (see Figure S3). Therefore, it can be concluded that $\alpha \sim 1$ when $D/L \gg 1$ and $\alpha \sim 0$ when $D/L \ll 1$. This observation is consistent with earlier experimental studies on long channel/pore ($D/L \ll 1$) that have shown almost no power-law dependence ($\alpha \approx 0$)[1,2,4] and nanopores with $D/L \gtrsim 1$ that have shown relatively high α values.[23,24,27] Figure 1D shows that $|\sigma|$ is proportional to the magnitude of the surface conductance but it has little effect on α. This observation is similar to the experimental observation on pH dependence of ionic conductance[1,17,26,31] where pH value has a small effect on α but pH value is directly related to the magnitude of the surface conductance. We note that α depends not only on the pore geometry but also on how the surface charges are distributed. When both the supporting membranes and the pore surface are charged, the α values are smaller than when only the pore surface is charged (see Figure 1A-B).

For an intuitive model, we consider the summation of the two limits, bulk and surface conductance, of Eq (11). At the high concentration limit, $|\tilde{\sigma}| \ll 1$, $G_{\mathrm{ph}} \sim G_{\mathrm{bulk}} = Fc_0(\mu_{\mathrm{ct}} +$

$\mu_{co}\left(\frac{L}{\pi R^2}+\frac{1}{2R}\right)^{-1}$, where μ_{ct} and μ_{co} are the counter-ion and co-ion mobility. At the low concentration limit, $\tilde{\sigma} \gg 1$, $G_{ph} \sim G_{surf} = Fc_0\mu_{ct}|2\tilde{\sigma}|^{1-\alpha}\left(\frac{L}{\pi R^2}+\frac{1}{2R}\right)^{-1}$. By adding these two limits, the electrophoretic conductance can be approximated as

$$G_{ph} \approx G_{bulk} + G_{surf} = Fc_0\{(1+|2\tilde{\sigma}|^{1-\alpha})\mu_{ct} + \mu_{co}\}\left(\frac{L}{\pi R^2}+\frac{1}{2R}\right)^{-1}. \quad (12)$$

The model in Eq 12 provides an intuitive understanding of ion transport through a charged pore. The dimensionless term, $|2\tilde{\sigma}|^{1-\alpha}$, represents the conductance enhancement due to the counterion transport in the diffuse layer. When $1 \gg |2\tilde{\sigma}|^{1-\alpha}$, the bulk transport is dominant and when $1 \ll |2\tilde{\sigma}|^{1-\alpha}$, the surface conductance is dominant. Eq (12) is a reasonable approximation to Eq (11) for $0 \leq \alpha \lesssim 0.7$.

Total conductance with electric-potential-leakage

In addition to the bulk and diffuse layer ion transport (electrophoresis), the total conductance is also affected by the water transport driven by the ionic migration (electroosmosis). The electroosmotic flow generates an ionic current due to the net charge of solution in the pore.[50] The electroosmotic transport can be incorporated into Eq 11 by using electroosmotic mobility μ_{eo}. Then, the total conductance can be written as

$$G = Fc_0\left\{(\mu_+ + \mu_{eo})\left(\sqrt{1+\tilde{\sigma}^2}+\tilde{\sigma}\right)^{1-\alpha} + (\mu_- - \mu_{eo})\left(\sqrt{1+\tilde{\sigma}^2}-\tilde{\sigma}\right)^{1-\alpha}\right\}\left(\frac{L}{\pi R^2}+\frac{1}{2R}\right)^{-1}. \quad (13)$$

Electroosmotic mobility enhances the counter-ion transport but reduces the co-ion transport. The direction of electroosmotic flow is considered in the sign of electroosmotic mobility, which is the opposite sign of the surface charge. The electroosmotic contribution to the total conductance (Eq 13) can be written as,

$$G_{eo} = Fc_0\mu_{eo}\left\{\left(\sqrt{1+\tilde{\sigma}^2}+\tilde{\sigma}\right)^{1-\alpha} - \left(\sqrt{1+\tilde{\sigma}^2}-\tilde{\sigma}\right)^{1-\alpha}\right\}\left(\frac{L}{\pi R^2}+\frac{1}{2R}\right)^{-1}. \quad (14)$$

This formulation is consistent with the fact that the electroosmotic current is generated by the net charge in the pore. At low concentration limit ($\tilde{\sigma} \gg 1$), the total surface conductance (including the electroosmotic component) is given by,

$$G_{\mathrm{surf}} = Fc_0\mu_{\mathrm{ct}}\left(1 + \frac{|\mu_{\mathrm{eo}}|}{\mu_{\mathrm{ct}}}\right)|2\tilde{\sigma}|^{1-\alpha}\left(\frac{L}{\pi R^2} + \frac{1}{2R}\right)^{-1}. \quad (15)$$

If μ_{eo} is assumed constant and independent of the reservoir concentration, G_{surf} has the same power-law exponent, α, as that of Eq 11 (see Figure S4). The dimensionless parameter $\frac{|\mu_{eo}|}{\mu_{ct}}$ is the enhancement factor in surface conductance due to the electroosmotic flow. In experimental situations, the surface charge density of the nanopore is generally unknown. Hence, the conductance theories are used to estimate the surface charge density by matching the theory with experimental conductance-concentration dataset.[1–4,26,31] We note that, the theory with electroosmosis predicts lower $|\sigma|$ than the theory without electroosmosis for a same conductance-concentration dataset. In the expression for electroosmotic conductance suggested by Levine *et al.,*[38] the electroosmotic mobility is given by, $|\mu_{eo}| = \frac{2\epsilon k_{\mathrm{B}}T}{\eta e}$, where η is the viscosity of the solution. This expression for electroosmotic mobility is suitable for non-overlapped (Electrical Double Layer) EDL system. Similarly, the electroosmotic mobility derived by Biesheuvel and Bazant[20] using SC theory[33] and Donnan equation is given by, $\mu_{\mathrm{eo}} = \frac{-\sigma R}{4\eta}$. This mobility is valid for highly overlapped EDL systems where the pore potential is almost invariant. Figure S10 shows the results from Eq (13) with these electroosmotic mobilities in comparison to all-atom MD and MD using implicit water. Those suggested electroosmotic mobilities shows a better prediction to the all-atom MD simulation. However, the electroosmotic mobility for electrically imperfect nanopore with slip is absent and further research is needed.

Ion selectivity

For a deeper understanding of ion transport in electrically imperfect/non-neutral nanopore, the contributions of each ion are investigated. Eq 13 can be decomposed into the contributions of cations and anions, *i.e.,* $G = G_+ + G_-$. Each contribution is given by,

$$G_\pm = Fc_0\left\{(\mu_\pm \pm \mu_{\mathrm{eo}})\left(\sqrt{1+\tilde{\sigma}^2} \pm \tilde{\sigma}\right)^{1-\alpha}\right\}\left(\frac{L}{\pi R^2}+\frac{1}{2R}\right)^{-1}. \quad (16)$$

The ion selectivity is defined as,

$$S_\pm \equiv \frac{G_\pm}{G}. \quad (17)$$

Using Eq 16 and 17, the ion selectivity can be calculated. Figure 4A-B show the contribution of counter-ion and co-ion conductance to total conductance, respectively. At high concentration, both K^+ and Cl^- ions contribute almost equally to the conductance. However, at low concentration the co-ion (Cl^-) contribution decays faster than that of counter-ions (K^+). As a result, at low concentration, the counter-ion transport governs ionic conductance. Moreover, the theory can also predict the ion selectivity of nanopore. Figure 4C shows that the ion selectivity obtained from MD and theory are in good agreement predicting that ion selectivity increases and approaches one as the concentration decreases. We note that electroosmosis is a important factor in the selective ion transport according to Eq 16-17 (see Figure S5).

Comparison with experimental data

The experimentally measured power-law exponents from various studies are shown in Figure 5A. It should be noted that physically α is the fraction of the surface-electric-potential that leaks out of the pore and mathematically α is the power-law exponent of surface conductivity. Most experimental data show a consistent behavior that α increases as R/L increases despite varying nanopore sizes (see Figure 5B). This consistency among the various independent experimental studies support the validity of the conductance model with electrically non-neutral or imperfect pores. In addition, the consistency among different materials can be understood as the surface

transport (for pore $D \gtrsim 3$ nm) is governed by the electrostatic force, which is characterized by the surface charge density, σ, in the model. The deviations observed for CNT data may imply that there could be other omitted physics. For example, the surface charge density of CNT immersed in the solution may depend on the reservoir concentration (charge regulation).[16,17,20–22] The α values obtained from MD simulation assume an ideal case of a perfect cylindrical geometry (no mechanical and chemical defects) with a homogeneous charge distribution. In this case, α can be empirically modeled as

$$\alpha \sim \frac{1}{\sqrt{\pi}} \left(\frac{L}{R} + \frac{1}{2} \right)^{-\frac{1}{2}}. \tag{18}$$

In practical cases, in addition to pore geometrical parameters, α can also be affected by the charge distribution. For sub-3nm pores or highly confined system, α can depend on the material type (*e.g.* SiO_2, Si_3N_4, *etc.*), as at these length scales, in addition to electrostatic interactions, van der Waals interactions and the finite size of the ions[51] also play an important role.

Finally, we tested the conductance theory for electrically imperfect nanopores given in Eqs 13 and 18 with the published experimental data. For this comparison, we assumed $\mu_{\mathrm{eo}} = 0$ due to the absence of electroosmotic mobility for electrically imperfect nanopore as we discussed earlier. Therefore, the actual surface charge density can be lower to some extent than the estimated value. Most of the experimental data are well described by the theory we present (see Figure 6). The estimated surface charge density of Si_3N_4 and SiO_2 are in the reasonable range compared to the typical value $\sigma \sim -20$ mC/m^2[52] and $\sigma \sim -100$ mC/m^2[53] respectively. In the case of small-diameter CNT, the estimated $|\sigma|$ is very large at high pH. One possible explanation of this is a strong osmotic current amplified by a large slip on the hydrophobic surface. The conductance model also describes the conductance of biological nanopores that have sub-3 nm

effective diameter. However, the quantitative estimation of surface charge density in sub-3 nm pore may require a comprehensive ion transport model including interfacial phenomena such as near-surface mobility/viscosity,[49,54] van der Waals type adsorption, finite size of ion on EDL[51] and wall/fluid slip.[55]

CONCLUSION

The net charge in the EDL near a pore surface is the source of the surface conductance. Our coarse-grained MD simulations demonstrate that various power-laws can be observed in pores with a constant surface charge. We also investigated the axial net charge distribution in the pore and conclude that there is leakage of surface-electric-potential from the pore into the reservoir. By considering the electrochemical equilibrium with the electric-potential-leakage, we developed an ion conductance theory that describes power-laws with exponents between zero and one. The ion conductance theory accounting for the leakage of surface-electrical-potential describes the conductance and selectivity obtained from MD simulation of nanopores of various lengths, diameters, and surface charge densities. Analysis of the published experimental and MD data reveals that the exponent of the power-law is related to the aspect ratio of the nanopore. An empirical model is proposed to describe the exponent of the power-law by using MD data on a perfect cylindrical pore and homogeneous surface charge. The ion conductance theory with empirical power-law relation describes well most of the experimental data.

METHODS

For ion transport studies, coarse-grained MD simulations were performed with implicit water and explicit ions. Utilizing implicit water enables us to perform several orders of magnitude more efficient ion transport studies compared to all-atom MD simulations as the number of atoms in the system are significantly reduced. The coarse-grained MD simulations implicitly consider the viscosity, thermal collision, hydration energy, distance-dependent dielectric permittivity, and therefore properly reproduces concentration dependent ion mobility, the ionic structure in the solution, and the ionic interfacial structure. The Langevin dynamics is used to generate the thermal motion of ions. The damping parameters of Langevin Dynamics are adjusted to reproduce the viscosity of the solution by matching the experimental ion mobility (for both K^+ and Cl^-) in a dilute solution (the Stokes' drag of ion, $\eta = \frac{qE}{6\pi\mu r}$, where E is electric field, r is radius of ion). We refer to an earlier study on the implicit water MD simulation done by Lenart *et al.*[56] for distance-dependent dielectric permittivity and hydration energy correction**.** The distance-dependent dielectric primitivity is modeled as $\epsilon_{\mathrm{d}}(r) = \frac{5.2+\epsilon_{\mathrm{s}}}{2} + \frac{\epsilon_{\mathrm{s}}-5.2}{2}\tanh\left(\frac{r-r_{\mathrm{me}}}{\sigma_{\epsilon}}\right)$, where ϵ_{s} is the bulk solution permittivity, r_{me} and σ_{ϵ} are free parameters representing the location of the first hydration shell and the distance scale of the permittivity recovery. This model assumes that most of the bulk dielectric permittivity is recovered after the first hydration shell. The hydration energy is modeled as a Gaussian function, $E_{\mathrm{hyd}} = \frac{H}{\sigma_{\mathrm{h}}\sqrt{2\pi}}\exp\left(-\frac{(r-r_{\mathrm{mh}})^2}{2\sigma_{\mathrm{h}}^2}\right)$, where H is the intensity factor of hydration energy, r_{mh} is mean and σ_{h} is standard deviation. In the original work, these free parameters were optimized by fitting concentration-dependent activity coefficient and Radial Distribution Function (RDF) of cation and anion. In the present study, all free parameters were re-optimized to reproduce the concentration dependence of molar

conductivity, $\Lambda(c_0)$, and RDFs of all ion pairs (see Figure S6 for optimization procedure). The molar conductivity and the RDFs obtained from the optimized potential are shown in Figure S7-8. Finally, EDL is reproduced by adjusting LJ potentials between ions and carbon (see Figure S9). The optimized force-field for implicit water and explicit ions is listed in Table S1. The benchmark study of ion transport using this potential is shown in Figure S10.

For ion transport studies using implicit water, a nanopore and two reservoirs attached to the edges of the pore were considered. Three reservoirs of sizes 35 nm, 50 nm and 70 nm cube are considered depending on the reservoir concentration (a lower concentration requires a larger reservoir). Aqueous KCl solution and a fixed cylindrical pore made of carbons is considered. The effective diameters of the pores were determined by subtracting the wall-fluid LJ diameter[57] from the center-to-center diameter of pore. The pore surface and membranes are homogeneously charged. We applied electric potential difference in the linear regime of current-voltage curve (less than 0.5 V). For electrically neutral systems, extra counterions are added to the system.[58] MD simulation is initially performed under the NVT ensemble for 20 ns to 100 ns with the electric field until the system reaches the steady state. Then, the atomic trajectories are integrated by the NVE ensemble. The time step is set to 10 fs and the data were obtained during 10 ns ~ 500 ns (lower concentrations require longer data collection time).

For all-atom MD simulation, SPC/E water[59] was utilized. The bond angle and length are maintained by the SHAKE algorithm.[60] The long-range Coulomb potential is computed by the PPPM method.[61] The interatomic interactions among the molecular pairs are modeled by the LJ potential. We used the optimized ion forcefield for use with SPC/E water.[62] We used the carbon-water interatomic potential reproducing a proper contact angle.[63] The rest of atomic pair potentials are modeled by the Lorentz-Berthelot mixing rule. The force-fields are summarized in

Table S2. The NVT ensemble is utilized for velocity integration with 2 fs time step. Nose-Hoover dynamics are employed to maintain the temperature by adjusting only the velocity components that are perpendicular to the electric field. The relatively small size reservoir, 15nm, is considered due to the high computational cost of all-atom MD. The other conditions are the same as those used in the implicit water model. For short and long range potential, GPU-accelerated calculation was utilized.[64,65]

The ion current is computed by counting the number of ions passing the pore. The Large-scale Atomic/Molecular Massively Parallel Simulator (LAMMPS)[66] is used for all simulations.

AUTHOR INFORMATION

Corresponding Author

*E-mail: aluru@illinois.edu

ORCID

Yechan Noh: 0000-0003-1688-4907

N. R. Aluru: 0000-0002-9622-7837

ACKNOWLEDGMENTS

We thank M. Herianian for valuable discussions on this work. The work on coarse-grained simulation of ion transport through nanopores was supported by the Center for Enhanced Nanofluidic Transport (CENT), an Energy Frontier Research Center funded by the U.S. Department of Energy, Office of Science, Basic Energy Sciences (DE-SC0019112). The other

aspects of the work presented here were supported by the National Science Foundation under Grants 1545907, 1708852, 1720633, and 1921578. The computing power is provided by the Extreme Science and Engineering Discovery Environment (XSEDE) granted by National Science Foundation (NSF) Grant No. OCI-1053575 and Blue Waters supercomputing center, awarded by the state of Illinois and NSF, OCI-0725070, ACI-1238993.

ASSOCIATED CONTENT

Supporting Information Available:

Additional details for ion conductance modeling (Figure S1-5), the development of implicit water forcefield (Figure S6-9), the benchmark study of MD simulations with SPC/E water and implicit water (Figure S10), the optimized forcefield of implicit water (Table S1), and the AAMD forcefield with SPC/E water (Table S2). This material is available free of charge *via* the Internet at http://pubs.acs.org.

LIST OF FIGURES

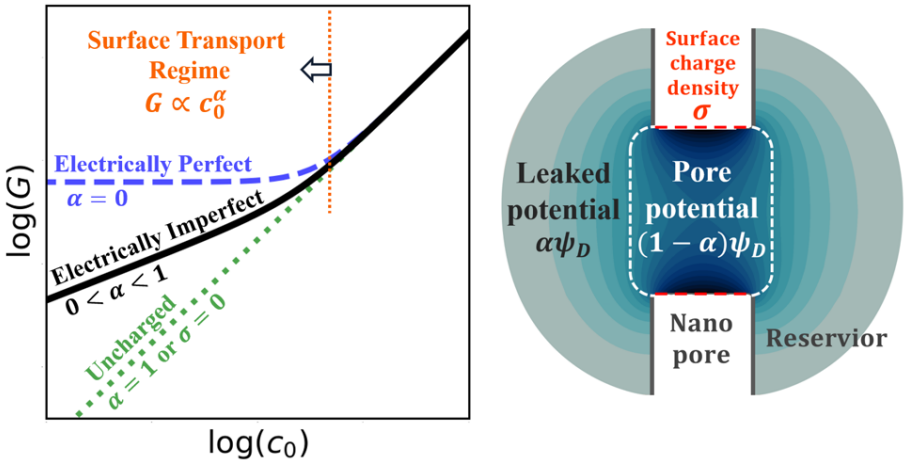

Table of Contents Graphic

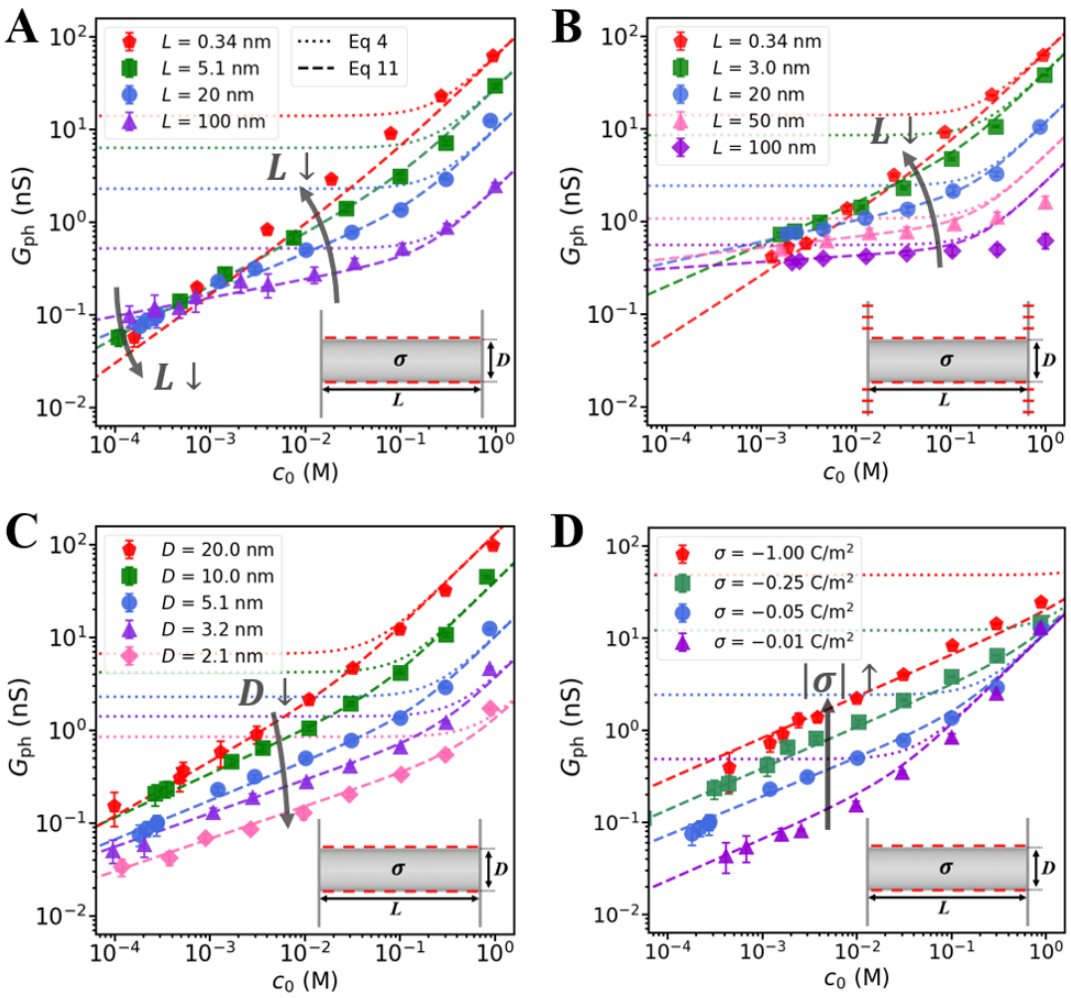

Figure 1. Ionic conductance *versus* reservoir ion concentration (G-c_0 curve). In (A-B), the pore length is varied, and the diameter and surface charge density are fixed, $D = 5.1$ nm and $\sigma = -50$ mC/m^2. In (C), diameter is varied and the pore length and surface charge density are fixed, $L = 20$ nm and $\sigma = -50$ mC/m^2. In (D), surface charge density is varied and pore length and diameter are fixed, $L = 20$ nm and $D = 5.1$ nm. As shown in the inset, only the pore surface is assumed to be charged in (A) and both the pore and membrane surface are assumed to be charged in (B). The best-fit curves of Eq 11 to the MD datasets are obtained by fitting α.

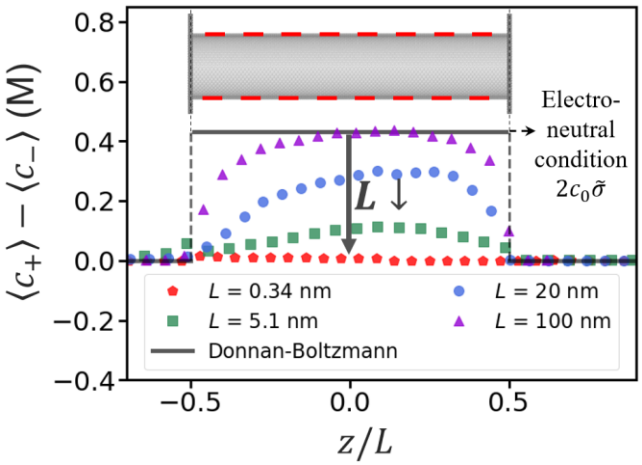

Figure 2. Axial distribution of the net charge concentration of solution inside the pore. The symbols represent MD simulation data obtained with $D = 5.1\,\mathrm{nm}$, $\sigma = -50\,\mathrm{mC/m^2}$, $c_0 = 0.03$ M and the length of the nanopore is varied. The external electric field is applied in the positive z-direction.

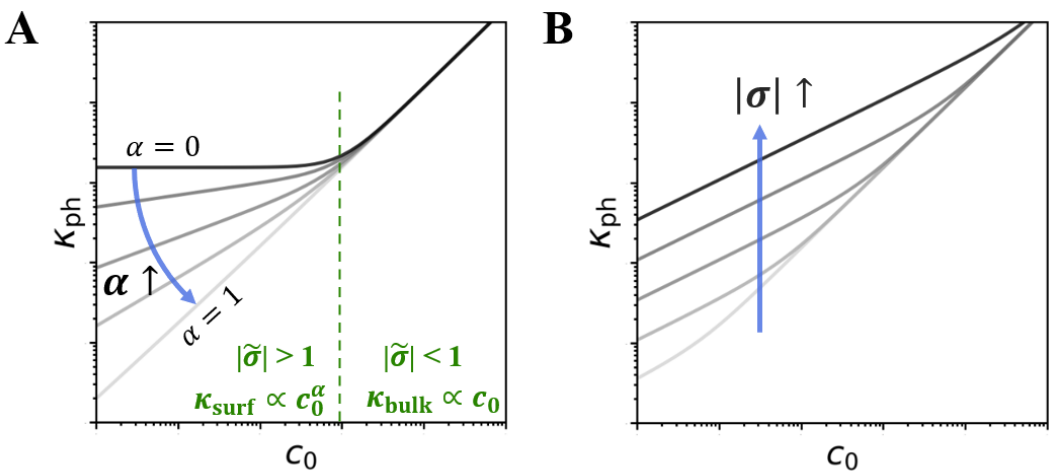

Figure 3. The role of α and σ in the ion conductivity theory given by Eq 10 (A) α is varied and σ is fixed (B) α is fixed and σ is varied.

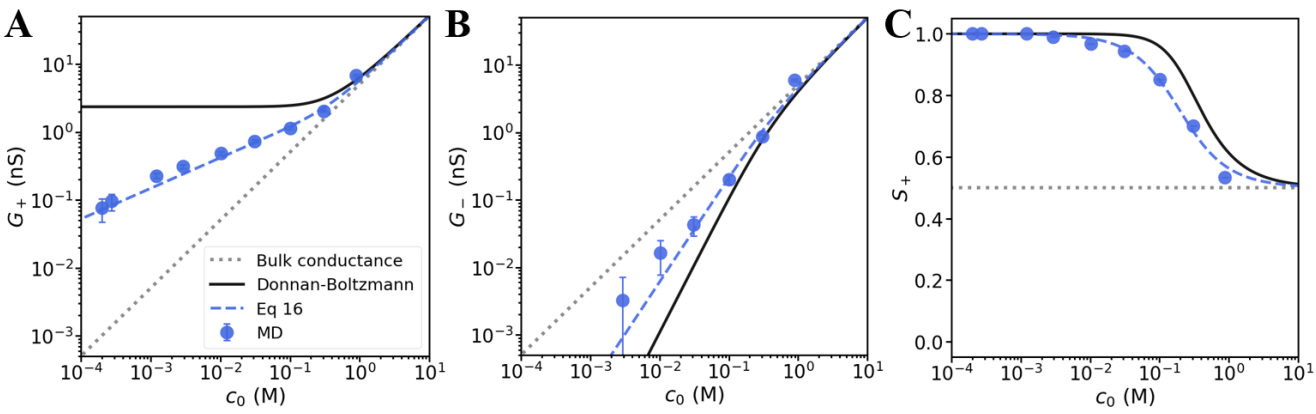

Figure 4. Contribution of counter-ion and co-ion to ionic conductance (A) counter-ion contribution (in this case $\sigma < 0$) and (B) co-ion contribution. (C) The ionic selectivity as a function of ion concentration. The all data are for nanopore with $L = 20$ nm, $D = 5.1$ nm, $\sigma = -50$ mC/m^2. In MD simulation, the selectivity is directly computed from the definition, $S \equiv G_+/G$. The bulk conductance and Donnan-Boltzmann prediction of conductance are special cases of Eq 16 with $\alpha = 1$ and $\alpha = 0$, respectively.

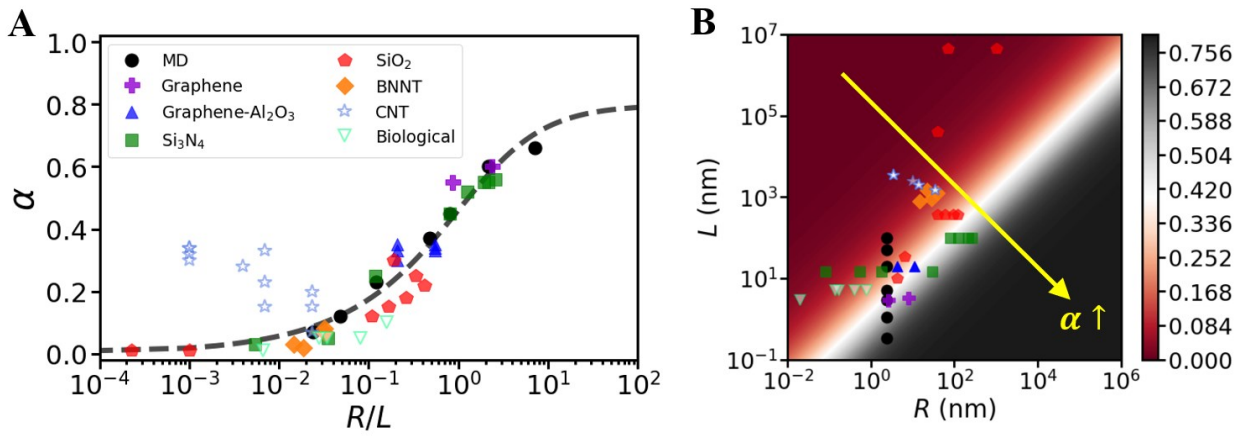

Figure 5. Power-law exponents relations obtained from MD and experiments. **(**A) The exponent of the power-law *versus* the aspect ratio of the pore (R/L or H/L for a rectangular channel). The exponent of the power-law is determined from the slope of the conductance-concentration curve in the log-log scale at low concentration. The dashed line is Eq 18. (B) A phase diagram of electrical imperfectness of nanopore determined by Eq 18 (color bar indicates α). The experimental datasets considered here include: Graphene,[24,25] Graphene-Al_2O_3,[26] Si_3N_4,[27] SiO_2,[16,28,29] BNNT,[2] CNT,[17] and biological nanopore.[32] For the MD data plotted here both the supporting membrane and the pore surface are charged.

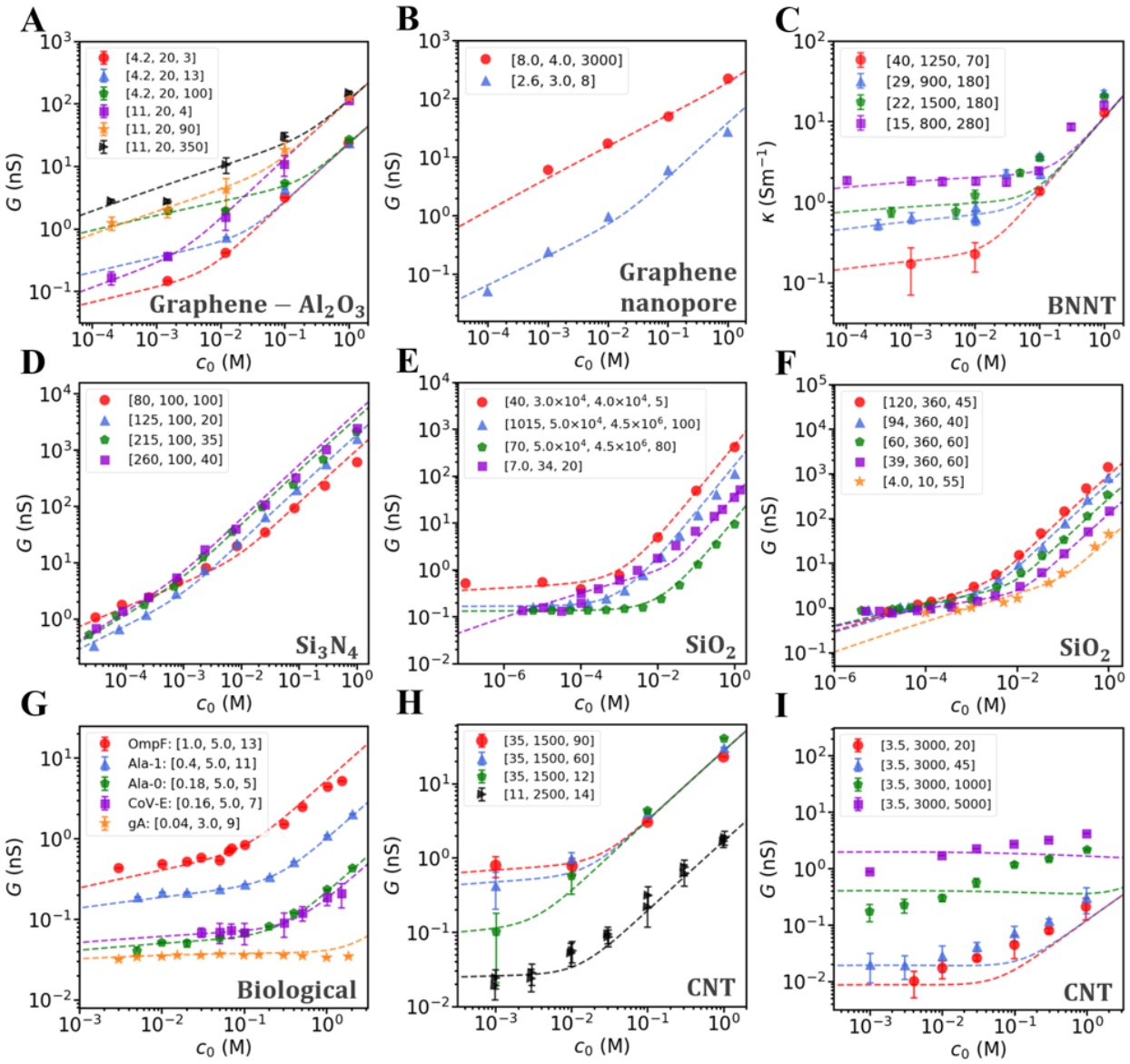

Figure 6. Conductance-concentration curves from various experiments and the conductance theory given in Eqs 13 and 18. Here, σ (the surface charge density) is the only fitting parameter in the theory. In (C) conductivity is plotted instead of conductance. The legend in each subplot shows $[R\ (\mathrm{nm}), L\ (\mathrm{nm}), |\sigma|\ (\mathrm{mC/m^2})]$ for circular pores and $[H\ (\mathrm{nm}), W\ (\mathrm{nm}), L\ (\mathrm{nm}), |\sigma|\ (\mathrm{mC/m^2})]$ for rectangular channels. The sources for experimental data are (A) Venkatesan *et al.*[26] (B) blue: Kumar *et al.*;[24] red: Shan *et al.*[25] (C) Siria *et al.*[2] (D) Lee *et al.*[27] (E) red: Martins *et al.*,[67] green/blue: Stein *et al.*;[1] violet: Smeets *et al.*[16] (F) orange:

Roy and Hall;[29] the remaining colors: Petrossian *et al.*[28] (G) Queralt-Martín *et al.*[32] (H-I) Secchi *et al.*[17]

REFERENCES

(1) Stein, D.; Kruithof, M.; Dekker, C. Surface-Charge-Governed Ion Transport in Nanofluidic Channels. *Phys. Rev. Lett.* **2004**, *93*, 035901.

(2) Siria, A.; Poncharal, P.; Biance, A.-L.; Fulcrand, R.; Blase, X.; Purcell, S. T.; Bocquet, L. Giant Osmotic Energy Conversion Measured in a Single Transmembrane Boron Nitride Nanotube. *Nature* **2013**, *494*, 455–458.

(3) Feng, J.; Graf, M.; Liu, K.; Ovchinnikov, D.; Dumcenco, D.; Heiranian, M.; Nandigana, V.; Aluru, N. R.; Kis, A.; Radenovic, A. Single-Layer MoS2 Nanopores as Nanopower Generators. *Nature* **2016**, *536*, 197.

(4) Radha, B.; Esfandiar, A.; Wang, F. C.; Rooney, A. P.; Gopinadhan, K.; Keerthi, A.; Mishchenko, A.; Janardanan, A.; Blake, P.; Fumagalli, L.; Lozada-Hidalgo, M.; Garaj, S.; Haigh, S. J.; Grigorieva, I. V.; Wu, H. A.; Geim, A. K. Molecular Transport through Capillaries Made with Atomic-Scale Precision. *Nature* **2016**, *538*, 222–225.

(5) Balme, S.; Picaud, F.; Manghi, M.; Palmeri, J.; Bechelany, M.; Cabello-Aguilar, S.; Abou-Chaaya, A.; Miele, P.; Balanzat, E.; Janot, J. M. Ionic Transport through Sub-10 Nm Diameter Hydrophobic High-Aspect Ratio Nanopores: Experiment, Theory and Simulation. *Sci Rep* **2015**, *5*, 1–14.

(6) Wen, C.; Zhang, Z.; Zhang, S.-L. Physical Model for Rapid and Accurate Determination of Nanopore Size *via* Conductance Measurement. *ACS Sens.* **2017**, *2*, 1523–1530.

(7) Jain, T.; Rasera, B. C.; Guerrero, R. J. S.; Boutilier, M. S. H.; O'Hern, S. C.; Idrobo, J.-C.; Karnik, R. Heterogeneous Sub-Continuum Ionic Transport in Statistically Isolated Graphene Nanopores. *Nature Nanotech* **2015**, *10*, 1053–1057.

(8) Heerema, S. J.; Dekker, C. Graphene Nanodevices for DNA Sequencing. *Nature Nanotech* **2016**, *11*, 127–136.

(9) Garaj, S.; Liu, S.; Golovchenko, J. A.; Branton, D. Molecule-Hugging Graphene Nanopores. *PNAS* **2013**, *110*, 12192–12196.

(10) Traversi, F.; Raillon, C.; Benameur, S. M.; Liu, K.; Khlybov, S.; Tosun, M.; Krasnozhon, D.; Kis, A.; Radenovic, A. Detecting the Translocation of DNA through a Nanopore Using Graphene Nanoribbons. *Nature Nanotech* **2013**, *8*, 939–945.

(11) Liu, K.; Feng, J.; Kis, A.; Radenovic, A. Atomically Thin Molybdenum Disulfide Nanopores with High Sensitivity for DNA Translocation. *ACS nano* **2014**, *8*, 2504.

(12) Xiao, K.; Jiang, L.; Antonietti, M. Ion Transport in Nanofluidic Devices for Energy Harvesting. *Joule* **2019**, *3*, 2364–2380.

(13) Esfandiar, A.; Radha, B.; Wang, F. C.; Yang, Q.; Hu, S.; Garaj, S.; Nair, R. R.; Geim, A. K.; Gopinadhan, K. Size Effect in Ion Transport through Angstrom-Scale Slits. *Science* **2017**, *358*, 511.

(14) Hong, S.; Constans, C.; Surmani Martins, M. V.; Seow, Y. C.; Guevara Carrió, J. A.; Garaj, S. Scalable Graphene-Based Membranes for Ionic Sieving with Ultrahigh Charge Selectivity. *Nano Lett.* **2017**, *17*, 728–732.

(15) Siria, A.; Bocquet, M.-L.; Bocquet, L. New Avenues for the Large-Scale Harvesting of Blue Energy. *Nat Rev Chem* **2017**, *1*, 1–10.

(16) Smeets, R. M. M.; Keyser, U. F.; Krapf, D.; Wu, M.-Y.; Dekker, N. H.; Dekker, C. Salt Dependence of Ion Transport and DNA Translocation through Solid-State Nanopores. *Nano Lett.* **2006**, *1*, 89–95.

(17) Secchi, E.; Niguès, A.; Jubin, L.; Siria, A.; Bocquet, L. Scaling Behavior for Ionic Transport and Its Fluctuations in Individual Carbon Nanotubes. *Phys. Rev. Lett.* **2016**, *116*, 154501.
(18) Gouy, M. Sur La Constitution de La Charge Électrique à La Surface d'un Électrolyte. *J. Phys. Theor. Appl.* **1910**, *9*, 457–468.
(19) Chapman, D. L. LI. A Contribution to the Theory of Electrocapillarity. *London, Edinburgh Dublin Philos. Mag. J. Sci.* **1913**, *25*, 475–481.
(20) Biesheuvel, P. M.; Bazant, M. Z. Analysis of Ionic Conductance of Carbon Nanotubes. *Phys. Rev. E* **2016**, *94*, 050601.
(21) Uematsu, Y.; Netz, R. R.; Bocquet, L.; Bonthuis, D. J. Crossover of the Power-Law Exponent for Carbon Nanotube Conductivity as a Function of Salinity. *J. Phys. Chem. B* **2018**, *122*, 2992–2997.
(22) Manghi, M.; Palmeri, J.; Yazda, K.; Henn, F.; Jourdain, V. Role of Charge Regulation and Flow Slip in the Ionic Conductance of Nanopores: An Analytical Approach. *Phys. Rev. E* **2018**, *98*, 012605.
(23) Rollings, R. C.; Kuan, A. T.; Golovchenko, J. A. Ion Selectivity of Graphene Nanopores. *Nat Commun* **2016**, *7*, 1–7.
(24) Kumar, A.; Park, K.-B.; Kim, H.-M.; Kim, K.-B. Noise and Its Reduction in Graphene Based Nanopore Devices. *Nanotechnology* **2013**, *24*, 495503.
(25) Shan, Y. P.; Tiwari, P. B.; Krishnakumar, P.; Vlassiouk, I.; Li, W. Z.; Wang, X. W.; Darici, Y.; Lindsay, S. M.; Wang, H. D.; Smirnov, S.; He, J. Surface Modification of Graphene Nanopores for Protein Translocation. *Nanotechnology* **2013**, *24*, 495102.
(26) Venkatesan, B. M.; Estrada, D.; Banerjee, S.; Jin, X.; Dorgan, V. E.; Bae, M.-H.; Aluru, N. R.; Pop, E.; Bashir, R. Stacked Graphene-Al2O3 Nanopore Sensors for Sensitive Detection of DNA and DNA–Protein Complexes. *ACS Nano* **2012**, *6*, 441–450.
(27) Lee, C.; Joly, L.; Siria, A.; Biance, A.-L.; Fulcrand, R.; Bocquet, L. Large Apparent Electric Size of Solid-State Nanopores Due to Spatially Extended Surface Conduction. *Nano Lett.* **2012**, *12*, 4037–4044.
(28) Petrossian, L.; Wilk, S. J.; Joshi, P.; Goodnick, S. M.; Thornton, T. J. Demonstration of Coulter Counting through a Cylindrical Solid State Nanopore. *J. Phys.: Conf. Ser.* **2008**, *109*, 012028.
(29) Roy, D. B.; Hall, A. R. Solid-State Nanopore Analysis of Alcohol-Soluble Molecules. *Analyst* **2017**, *142*, 1676–1681.
(30) Pang, P.; He, J.; Park, J. H.; Krstić, P. S.; Lindsay, S. Origin of Giant Ionic Currents in Carbon Nanotube Channels. *ACS Nano* **2011**, *5*, 7277–7283.
(31) Yao, Y.-C.; Taqieddin, A.; Alibakhshi, M. A.; Wanunu, M.; Aluru, N. R.; Noy, A. Strong Electroosmotic Coupling Dominates Ion Conductance of 1.5 Nm Diameter Carbon Nanotube Porins. *ACS Nano* **2019**, *13*, 12851–12859.
(32) Queralt-Martín, M.; López, M. L.; Aguilella-Arzo, M.; Aguilella, V. M.; Alcaraz, A. Scaling Behavior of Ionic Transport in Membrane Nanochannels. *Nano Lett.* **2018**, *18*, 6604–6610.
(33) Peters, P. B.; van Roij, R.; Bazant, M. Z.; Biesheuvel, P. M. Analysis of Electrolyte Transport through Charged Nanopores. *Phys. Rev. E* **2016**, *93*, 053108.
(34) Gross, R. J.; Osterle, J. F. Membrane Transport Characteristics of Ultrafine Capillaries. *J. Chem. Phys.* **1968**, *49*, 228–234.

(35) Bocquet, L.; Charlaix, E. Nanofluidics, from Bulk to Interfaces. *Chem. Soc. Rev.* **2010**, *39*, 1073–1095.
(36) Lipowsky, R.; Sackmann, E. *Structure and Dynamics of Membranes*; Elsevier: Amsterdam, 1995; pp 603–642.
(37) Khair, A. S.; Squires, T. M. Surprising Consequences of Ion Conservation in Electro-Osmosis over a Surface Charge Discontinuity. *J. Fluid Mech.* **2008**, *615*, 323–334.
(38) Levine, S.; Marriott, J. R.; Robinson, K. Theory of Electrokinetic Flow in a Narrow Parallel-Plate Channel. *J. Chem. Soc., Faraday Trans. 2* **1975**, *71*, 1–11.
(39) Schoch, R. B.; Renaud, P. Ion Transport through Nanoslits Dominated by the Effective Surface Charge. *Appl. Phys. Lett.* **2005**, *86*, 253111.
(40) Hall, J. E. Access Resistance of a Small Circular Pore. *J Gen Physiol* **1975**, *66*, 531–532.
(41) Sahu, S.; Zwolak, M. Maxwell-Hall Access Resistance in Graphene Nanopores. *Phys. Chem. Chem. Phys.* **2018**, *20*, 4646–4651.
(42) Maxwell, J. C. *A Treatise on Electricity and Magnetism*; Clarendon Press: Oxford, 1873; pp 353–359.
(43) Ghosal, S.; Sherwood, J. D.; Chang, H.-C. Solid-State Nanopore Hydrodynamics and Transport. *Biomicrofluidics* **2019**, *13*, 011301.
(44) Wang, L.; Boutilier, M. S. H.; Kidambi, P. R.; Jang, D.; Hadjiconstantinou, N. G.; Karnik, R. Fundamental Transport Mechanisms, Fabrication and Potential Applications of Nanoporous Atomically Thin Membranes. *Nat. Nanotechnol.* **2017**, *12*, 509–522.
(45) Sherwood, J. D.; Mao, M.; Ghosal, S. Electroosmosis in a Finite Cylindrical Pore: Simple Models of End Effects. *Langmuir* **2014**, *30*, 9261–9272.
(46) Levy, A.; de Souza, J. P.; Bazant, M. Z. Breakdown of Electroneutrality in Nanopores. *J. Colloid Interface Sci.* **2020**, *579*, 162–176.
(47) Chein, R.; Chen, H.; Liao, C. Investigation of Ion Concentration and Electric Potential Distributions in Charged Membrane/Electrolyte Systems. *J. Membr. Sci.* **2009**, *342*, 121–130.
(48) Tian, H.; Zhang, L.; Wang, M. Applicability of Donnan Equilibrium Theory at Nanochannel–Reservoir Interfaces. *J. Colloid Interface Sci.* **2015**, *452*, 78–88.
(49) Suk, M. E.; Aluru, N. R. Ion Transport in Sub-5-Nm Graphene Nanopores. *J. Chem. Phys.* **2014**, *140*, 084707.
(50) Karniadakis, G.; Beskok, A.; Aluru, N. *Microflows and Nanoflows Fundamentals and Simulation;* Springer: New York, 2005; pp 255–272.
(51) Qiao, R.; Aluru, N. R. Ion Concentrations and Velocity Profiles in Nanochannel Electroosmotic Flows. *J. Chem. Phys.* **2003**, *118*, 4692–4701.
(52) Sonnefeld, J. Determination of Surface Charge Density Parameters of Silicon Nitride. *Colloids Surf., A* **1996**, *108*, 27–31.
(53) Iler, R. K. *The Chemistry of Silica*; Wiley: New York, 1979; pp 659–665.
(54) Evans, D. J.; Hoover, W. G. Flows Far From Equilibrium *via* Molecular Dynamics. *Annu. Rev. Fluid Mech.* **1986**, *18*, 243–264.
(55) Thompson, P. A.; Troian, S. M. A General Boundary Condition for Liquid Flow at Solid Surfaces. *Nature* **1997**, *389*, 360–362.
(56) Lenart, P. J.; Jusufi, A.; Panagiotopoulos, A. Z. Effective Potentials for 1:1 Electrolyte Solutions Incorporating Dielectric Saturation and Repulsive Hydration. *J Chem Phys* **2007**, *126*, 044509.

(57) Noh, Y.; Vo, T.; Kim, B. Subatomic-Level Solid/Fluid Boundary of Lennard-Jones Atoms: A Molecular Dynamics Study of Metal-Inert Fluid Interface. *Appl. Sci.* **2019**, *9*, 2439.
(58) Celebi, A. T.; Beskok, A. Molecular and Continuum Transport Perspectives on Electroosmotic Slip Flows. *J. Phys. Chem. C* **2018**, *122*, 9699–9709.
(59) Berendsen, H.; Grigera, J. R.; Straatsma, T. P.; Grigera, J. R.; Straatsma, T. P.; Berendsen, H. J. C.; Grigera, J. R.; Straatsma, T. P.; Grijera, J. R.; Berendsen, H. J. C.; Grigerra, J. R.; Strsstsma, T. P.; Berendsen, C. The Missing Term in Effective Pair Potentials. **1987**.
(60) Ryckaert, J.-P.; Ciccotti, G.; Berendsen, H. J. C. Numerical Integration of the Cartesian Equations of Motion of a System with Constraints: Molecular Dynamics of *n*-Alkanes. *Journal of Computational Physics* **1977**, *23*, 327–341.
(61) Hockney, R. W.; Eastwood, J. W. *Computer Simulation Using Particles*; Taylor and Francis: New York, 1988; p 564.
(62) Joung, I. S.; Cheatham, T. E. Determination of Alkali and Halide Monovalent Ion Parameters for Use in Explicitly Solvated Biomolecular Simulations. *J. Phys. Chem. B* **2008**.
(63) Wu, Y.; Aluru, N. R. Graphitic Carbon–Water Nonbonded Interaction Parameters. *J. Phys. Chem. B* **2013**, *117*, 8802–8813.
(64) Brown, W. M.; Wang, P.; Plimpton, S. J.; Tharrington, A. N. Implementing Molecular Dynamics on Hybrid High Performance Computers – Short Range Forces. *Comput. Phys. Commun.* **2011**, *182*, 898–911.
(65) Brown, W. M.; Kohlmeyer, A.; Plimpton, S. J.; Tharrington, A. N. Implementing Molecular Dynamics on Hybrid High Performance Computers – Particle–Particle Particle-Mesh. *Comput. Phys. Commun.* **2012**, *183*, 449–459.
(66) Plimpton, S. Fast Parallel Algorithms for Short-Range Molecular Dynamics. *J. Comput. Phys.* **1995**, *117*, 1–19.
(67) Martins, D. C.; Chu, V.; Conde, J. P. The Effect of the Surface Functionalization and the Electrolyte Concentration on the Electrical Conductance of Silica Nanochannels. *Biomicrofluidics* **2013**, *7*, 034111.